Proceedings of the 21st ICSMGE, Vienna, Austria, 14 – 19 June 2026. Pistrol, Adam & Schweiger (eds.)
Published by: ÖGG, Austrian Society for Geomechanics, Salzburg, Austria, ISBN 978-3-9503898-4-5
https://doi.org/10.53243/ICSMGE2026-178

Investigation of the Predictive Accuracy of an Advanced Constitutive Model for Earthquake-Induced Excitations

Moritz Meyer, Lukas Knittel
Chair of Geotechnics, Institute of Civil Engineering, University of Applied Sciences and Arts Northwestern Switzerland, Switzerland, moritz.meyer@fhnw.ch

Merita Tafili, Torsten Wichtmann
Chair of Soil Mechanics, Foundation Engineering and Environmental Geotechnics, Ruhr-University Bochum, Bochum, Germany

ABSTRACT: This study evaluates the predictive performance of the Simple Anisotropic Sand (Sanisand) constitutive model for earthquake-induced loading of loosely compacted sand from an open-cast lignite mine. Model parameters were calibrated against monotonic and cyclic triaxial reference tests. The calibrated model was subsequently validated through simulations of undrained triaxial tests under vertical loading with both regular and irregular loading amplitudes, as well as through undrained hollow cylinder tests under cyclic torsional loading with regular amplitude. By comparing numerical results with laboratory tests, key insights and limitations emerge. For regular loading, the constitutive model reproduced the general cyclic response, with improved pore water pressure predictions at higher amplitudes. Under irregular loading, characteristic features were less accurately represented, while in hollow cylinder tests, the torsional cyclic response was captured with minor deviations.

KEYWORDS: earthquake-induced excitation; Simple Anisotropic Sand (Sanisand) constitutive model; numerical simulations; hollow cylinder tests; irregular loading signals

1 INTRODUCTION

Fundamental research on evaluating the potential for soil liquefaction induced by earthquake ground shaking has been conducted by various authors, most notably by (Seed & Idriss, 1971), (Ishihara & Yasuda, 1972) and (Ishihara & Yasuda, 1975). Investigations into the liquefaction resistance of an open-cast lignite mine soil from the Renish mining area in Germany under loading by earthquake-typical signals were conducted by (Knittel, et al., 2024), following the approach of (Ishihara & Yasuda, 1975), who examined the conversion of an earthquake-like, irregular signal into a regular signal with constant amplitude.

Numerical analyses of slope systems under seismic excitation, using dynamic finite element simulations, require constitutive models capable of realistically representing soil behavior - particularly pore water pressure accumulation - under earthquake-like conditions. Most advanced constitutive models that describe cyclic soil behavior were developed and validated based on tests with constant amplitude.

In this study, one of the most widely used advanced constitutive models in geotechnical engineering is examined, the Simple Anisotropic Sand (Sanisand) model proposed by Dafalias and Manzari (2004). The model parameters were first calibrated against reference laboratory tests (Sec. 4). Based on these parameters, selected undrained triaxial tests with vertical loading and regular signals (Sec. 5.1) as well as irregular signals (Sec. 5.2) were conducted. In addition, hollow cylinder triaxial tests with torsional loading and regular signals (Sec. 5.3) were numerically simulated for evaluate the model's capability to reproduce the liquefaction behavior of an open-cast mine sand. The numerical results were subsequently compared with laboratory data to assess the model's predictive accuracy.

2 OPEN-CAST LIGNITE MINE SOIL

The tested open-cast lignite mine soil material is characterized by a fine content FC of 4.13%, a mean grain diameter of d_{50} = 0.18 mm, and a coefficient of uniformity $C_u = d_{60}/d_{10}$ = 2.4. The grain density ϱ_s = 2.65 g/cm^3. Furthermore, the maximum and minimum void ratios are $e_{\max}$ = 1.091 and $e_{\min}$ = 0.670, respectively. The critical friction angle of the soil was determined to be φ'_c = 34.4°. Additional material properties can be found in (Knittel, et al., 2024). All triaxial and hollow cylinder tests were performed on samples prepared by moist tamping.

3 SIMPLE ANISOTROPIC SAND (SANISAND) MODEL

The most used version of the Sanisand models' family is the one developed by (Dafalias & Manzari, 2004), which will be adopted in the following analysis. It introduces a 'wedge'-type yield surface in p-q space obeying the following relationship:

$$f = [(\boldsymbol{s} - p\boldsymbol{\alpha}):(\boldsymbol{s} - p\boldsymbol{\alpha})]^{1/2} - \sqrt{2/3}pm = 0$$

where $\boldsymbol{s}$ is the deviatoric stress tensor, $\boldsymbol{\alpha}$ is the back stress ratio tensor and m is a material parameter defining the opening of the yield wedge. The model incorporates critical state concepts and bounding surface plasticity, allowing it to capture important features of sand behavior such as stress-induced anisotropy, fabric evolution, and cyclic mobility.

To account explicitly for the influence of evolving fabric on dilatancy, a tensorial state variable $\boldsymbol{z}$, referred to as fabric-dilatancy tensor, is introduced. The elasto-plastic (subscript "ep") stress-strain relationship is then governed by the following general rate equation $\dot{\boldsymbol{\sigma}} = \boldsymbol{E}^{\mathrm{ep}}(\boldsymbol{\sigma}, \boldsymbol{\alpha}, \mathbf{z}, \mathrm{e}, \dot{\boldsymbol{\varepsilon}}): \dot{\boldsymbol{\varepsilon}}$, with the elastoplastic tangent stiffness tensor $\boldsymbol{E}^{\mathrm{ep}}$. e is the void ratio and $\dot{\boldsymbol{\varepsilon}}$ is the strain rate tensor. The combination of the wedge-type yield surface, kinematic hardening via $\boldsymbol{\alpha}$, and fabric-dilatancy coupling via $\boldsymbol{z}$ enables the Sanisand model to simulate a wide range of monotonic and cyclic sand responses, including liquefaction phenomena under complex loading paths. For comprehensive mathematical derivations and parameter definitions, the reader is referred to (Dafalias & Manzari, 2004).

4 CALIBRATION OF MATERIAL PARAMETERS

The presented material model was calibrated on different experimental tests, such as oedometric compression tests, undrained (Figure 1a and 1b) and drained monotonic triaxial tests, and undrained cyclic triaxial tests (Figure 1c to 1f). All simulations were carried out using the Incremental Driver software, which was developed by (Niemunis, 2008) in combination with the user defined material routine (UMAT) which was provided by M. Tafili for Sanisand model. Fifteen material parameters were calibrated with the final set representing an average of the best-fit values, as shown in Table 1.

Table 1. Sanisand material parameters for the open-pit soil material

G_0 [-]	ν [-]	M_c [-]	M_e/M_c [-]		e_0 [-]	λ_c [-]	ξ [-]
150	0.20	1.128	0.70		1.04	0.137	0.405
n_d [-]	A_0 [-]	n_b [-]	h_0 [-]	c_h [-]	m [-]	c_z [-]	$z_{\max}$ [-]
1.50	0.30	1.50	6.00	0.65	0.05	1000	25

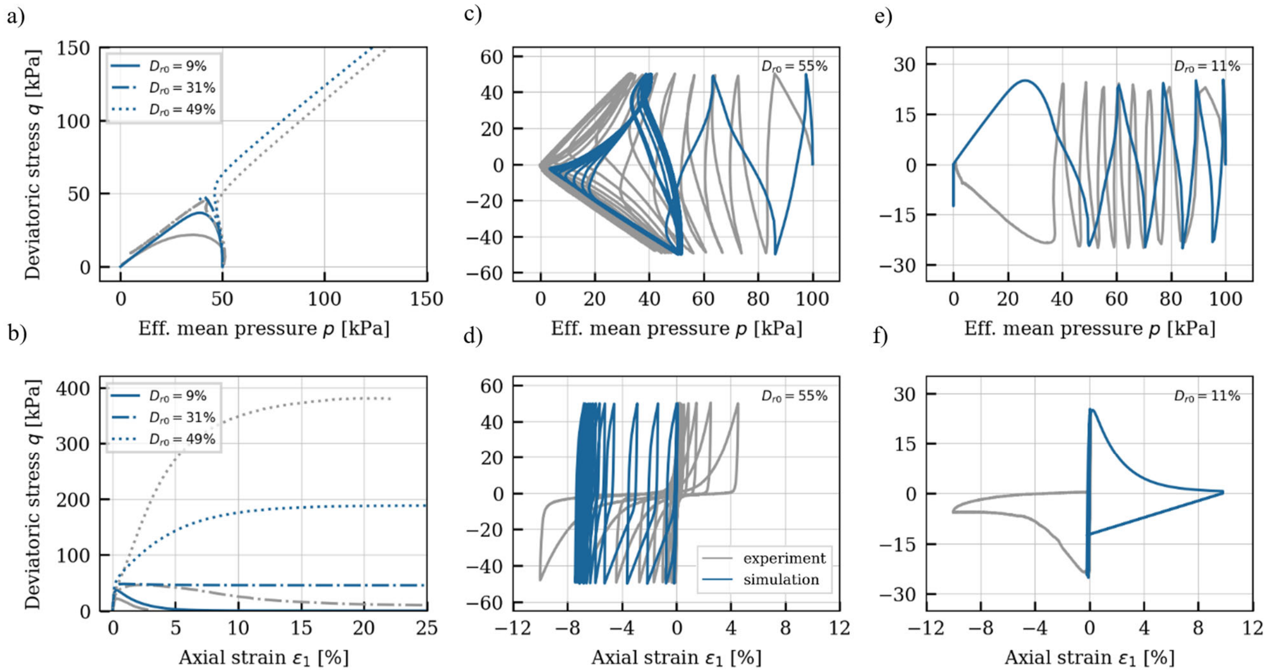

Figure 1. Simulations of undrained monotonic triaxial tests a,b) with different initial densities D_{r0} = 9%, 31% and 49% and an initial mean effective pressure p_0 = 50 kPa as well as undrained triaxial tests under cyclic loading with initial densities c,d) D_{r0} = 55% and e,f) D_{r0} = 11%, started from an initial mean effective pressure p_0 = 100 kPa.

Figures 1a and 1b present the monotonic undrained triaxial tests and corresponding model simulations at three initial relative densities, D_{r0}, ranging from very loose to medium density. While the effective stress paths in Figure 1a show good agreement between simulations and experiments, the deviatoric stress-axial strain curves in Figure 1b exhibit a less satisfactory match. This can be attributed, on the one hand, to the findings of (Wichtmann, et al., 2019), who demonstrated that the model parameters cannot be fully calibrated in a density-independent manner, and, on the other hand, to the fact that the tested sand contains 4.13% fine, which is not negligible and may influence its behavior. Consequently, the very loose specimens from the monotonic and cyclic triaxial tests were not fully considered in the calibration. Instead, the parameters were slightly adjusted to better reproduce the cyclic triaxial response of the medium-dense sample with D_{r0} = 55%.

Figures 1c and 1d show undrained cyclic triaxial tests on specimens with an initial relative density of D_{r0} = 55%, while Figures 1e and 1f present tests on specimens with D_{r0} = 11%. In both density cases, the simulations predict liquefaction occurring earlier than in the experiments. Nevertheless, the selected model parameters provide the best overall agreement on average across all simulations when compared to the experimental results.

5 MECHANICAL MODELLING OF TRIAXIAL TESTS

The test procedures and a more in-depth discussion of the laboratory test results are provided in the original publication from (Knittel, et al., 2024).

5.1 *Triaxial tests with regular signals*

Table 2 lists selected undrained cyclic triaxial tests under isotropic consolidation q_s = 0 kPa with regular deviatoric stress amplitudes q^{ampl}. The triaxial test series with regular signals R01-03 are shown in Figure 2 and R04-06 are in Figure 3. The results are presented in the effective stress paths in the p-q-plane (Figure 2a, 2c, 2e) and Figure 3a, 3c, 3e) and in the q-ε_1-diagram (Figure 2b, 2d, 2f and Figure 3b, 3d, 3f).

In the final phase of the tests, indications of cyclic mobility with characteristic "butterfly-shaped" stress paths can be observed in the simulation; however, due to the relatively loose condition of the samples, this pattern is not particularly pronounced in the experiment. In the laboratory experiment when the effective stress path approaches the failure envelope - a significant increase in strain amplitudes is observed. This behavior is seen in the stress-strain diagrams (q-ε_1), see Figure 3b, 3d, 3f and Figure 4b, 4d, 4f.

The simulations overestimate the strain accumulation during extension (q < 0) and underestimate the one during compression (q > 0) when compared to the experiment. Higher loading amplitudes lead to more extensive axial strain accumulation and fewer cycles required to reach liquefaction, reflecting a softer response in both experiments and simulations.

Figure 4 compares the measured and simulated evolution of the normalized excess pore water pressure $u^{\mathrm{acc}}(N)\ /p_0$ from the test series. The simulations revealed that with increasing loading amplitude, the pore water pressure response was captured better, leading to improved agreement with the experimental data. However, the Sanisand model consistently overestimates the rate of excess pore water pressure accumulation, reaching critical values in fewer cycles.

Table 2. Triaxial tests with regular signals R01-06, initial effective mean pressure p_0 = 100 kPa and isotropic consolidation q_s = 0 kPa

Test	R01	R02	R03	R04	R05	R06
D_{r0} [%]	35	34	29	36	35	33
q^{ampl} [kPa]	15	20	25	25	30	35

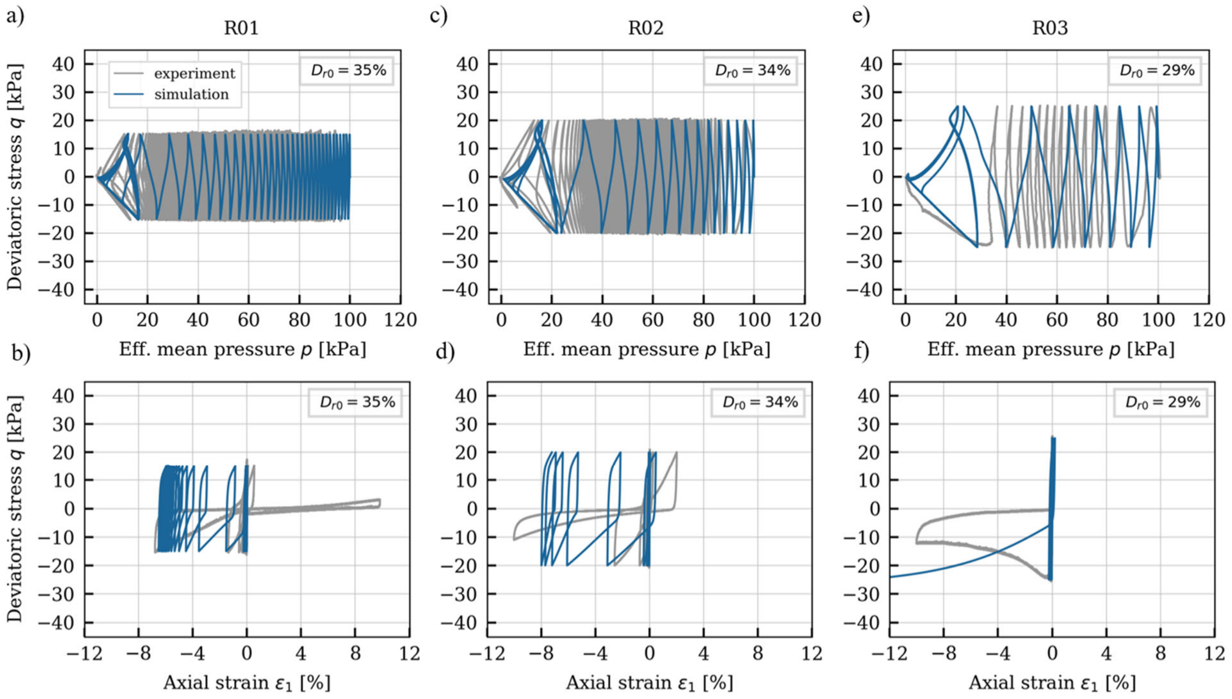

Figure 2. Sanisand simulations (blue) of triaxial tests with regular signals R01, R02, R03 (D_{r0} ≅ 30% and p_0 = 100 kPa) and q^{ampl} = a,b) 15 kPa, c,d) 20 kPa and e,f) 25 kPa.

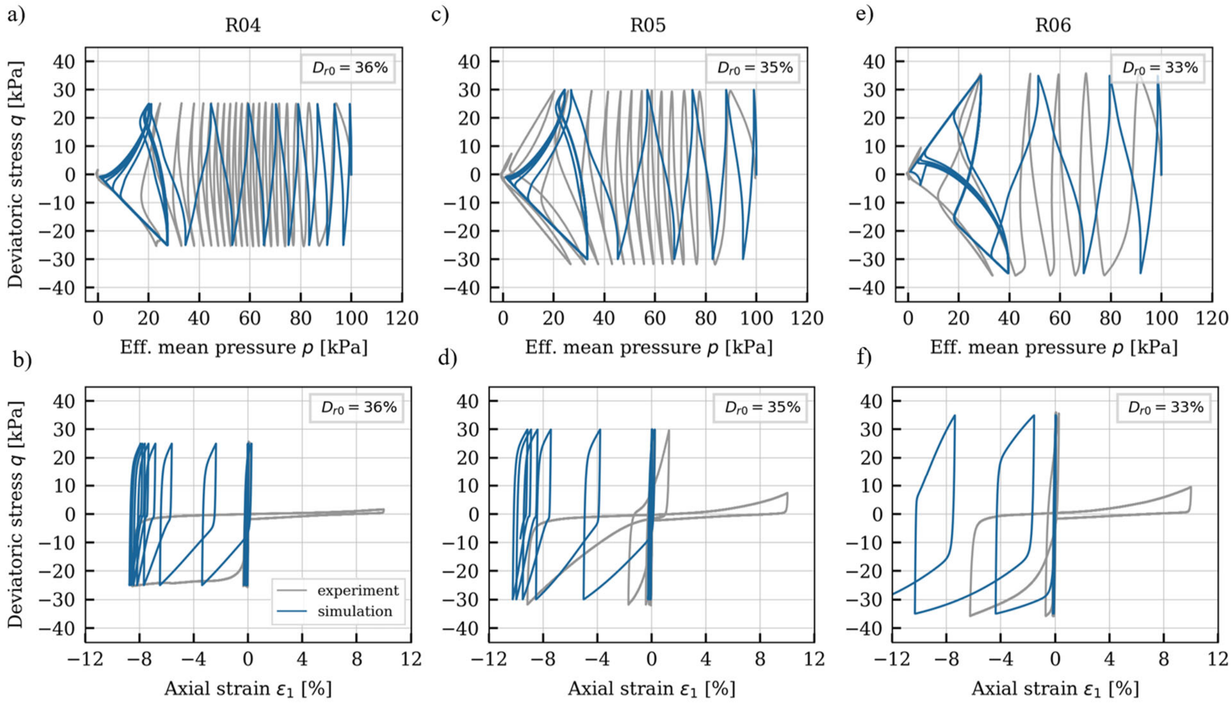

Figure 3. Sanisand simulations (blue) of triaxial tests with regular signals R04, R05, R06 (D_{r0} ≅ 30% and p_0 = 100 kPa) and q^{ampl} = a,b) 25 kPa, c,d) 30 kPa and e,f) 35 kPa

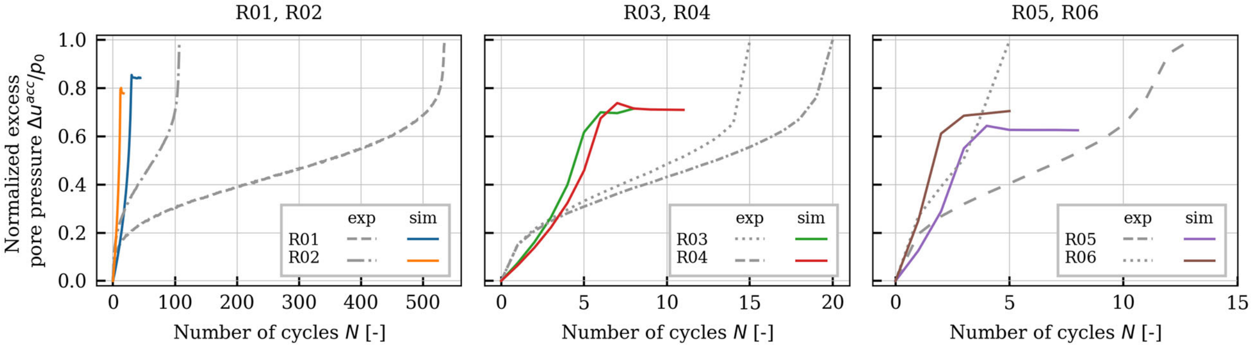

Figure 4. Sanisand simulations (colored) compared to experiments (grey) of the normalized excess pore water pressure $u^{\text{acc}}(N)/p_0$

5.2 *Triaxial tests with irregular signals*

Table 3 summarizes triaxial tests with irregular signals under isotropic consolidation, including IR15 and IR16 with slightly different $q^{\max}$ peaks, and IR17 and IR18 with mirrored earthquake signals. The initial stress state is isotropic q_s = 0 kPa. The laboratory tests were conducted using an earthquake-type excitation signal, with loading controlled by the deviatoric stress q. In the experiment IR15 and IR17 (Figure 5a with $q^{\max}$ = 40 kPa and 5c with 35 kPa) liquefaction did not occur, while in IR16 and IR18 (Figure 5b with $q^{\max}$ = 42 kPa and 5d with 37 kPa), liquefaction was observed. For details, see (Knittel, et al., 2024).

Table 3. Triaxial tests with irregular signals IR15-18 initial effective mean pressure p_0 = 100 kPa and isotropic consolidation q_s = 0 kPa

Test	IR15	IR16	IR17	IR18
D_{r0} [%]	31	32	30	31
q^{ampl} [kPa]	40	42	35	37
Direction of $q^{\max}$	compression		extension	

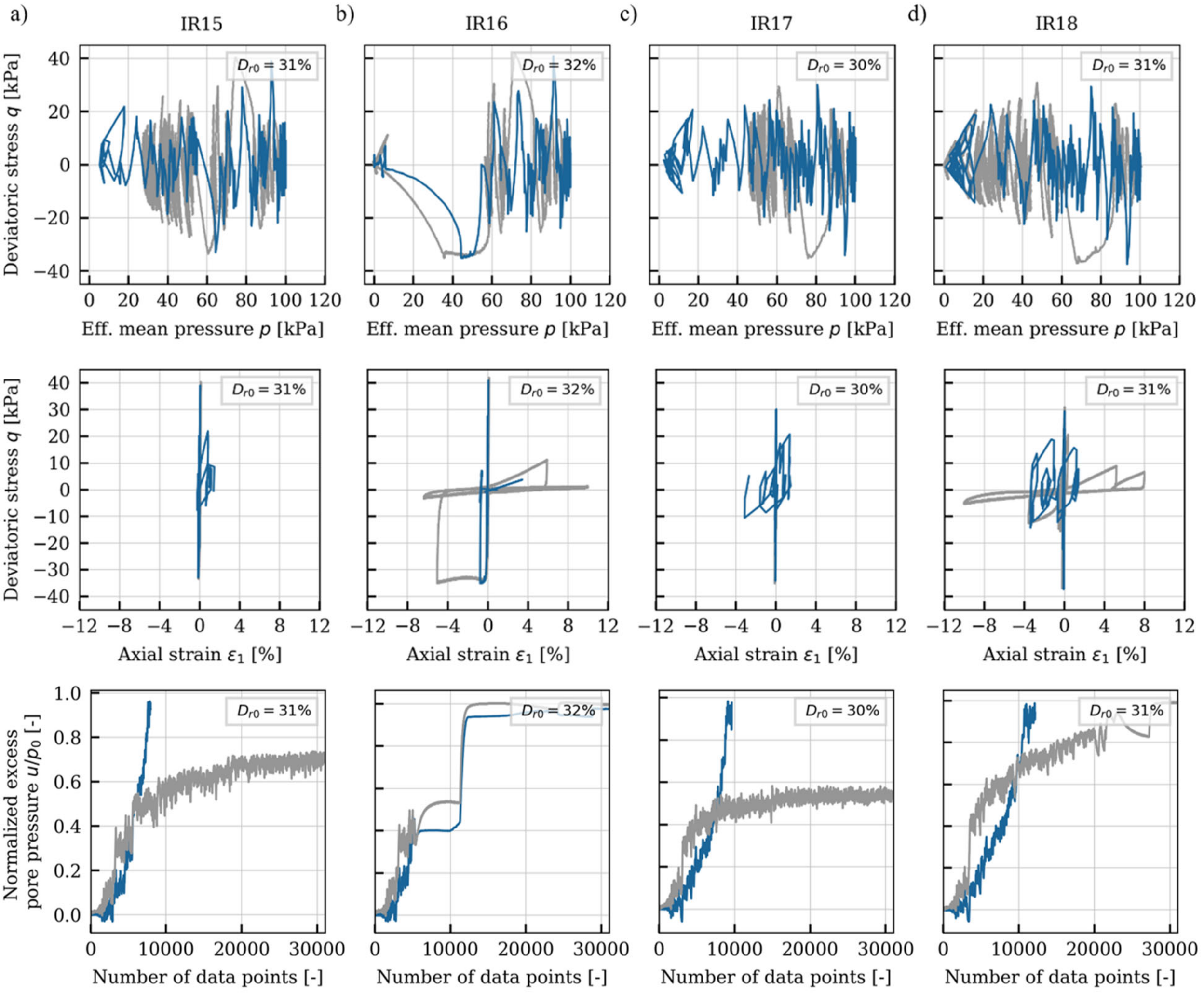

Figure 5. Sanisand simulations (blue) of triaxial tests IR15 to IR18 ($D_{r0} \cong 30\%$ and p_0 = 100 kPa) with irregular amplitudes. As well as the comparison of the simulations (colored) compared to experiments (grey) for the normalized excess pore water pressure u/p_0.

For the simulation results, the effective stress paths in the p-q-plane and the stress-strain paths in the q-ε_1 diagram are shown, see the first two rows in Figure 5. The plots in the lowest row in Figure 5 compares the measured and simulated evolution of the normalized excess pore water pressure u^{acc}/p_0 in from the irregular test series.

In the simulations for irregular loading, the characteristic short-term fluctuations ("jitter") in the response are not fully reproduced, and the liquefaction is generally overpredicted. Moreover, for smaller shear stress amplitudes differences (IR15 compared to IR16 and IR17 to IR18 in Figure 5a to 5c and 5b to 5d), the simulations were unable to clearly distinguish between cases with and without liquefaction and therefore the effective mean pressure dropped to zero in every simulated triaxial test with irregular signals.

The simulations in the q-ε_1-plane reveal the same behavior as observed for the regular signals: In the initial stages of irregular loading, axial strain remains nearly constant at zero, indicating negligible accumulation. As the mean effective pressure path approaches the failure envelope, axial strain accumulation increases progressively.

In IR15 and IR17 (Figure 5a and 5c), experiments did not reach liquefaction, whereas simulations predicted delayed pore pressure accumulation followed by rapid build-up to liquefaction and the effective mean pressure yields to zero. In IR16 and IR18 (Figure 5b and 5d), liquefaction occurred in both experiments and simulations, but the simulated pore pressure increase began later than in the experiments. It was observed that simulations of the irregular loading tests using Sanisand exhibited an overly soft response in the excess PWP. The simulated PWP evolution for test IR16 (Figure 5b) shows a good agreement with the experimental derived excess pore pressure.

The results indicate that the Sanisand model has limitations in fully capturing the characteristic soil response to irregular loading sequences

5.3 *Hollow cylinder triaxial tests with regular signals*

Table 4 presents an overview of the chosen test series with regular loading in the hollow cylinder triaxial apparatus with isotropic consolidation $\tau_s = 0$ kPa. The simulations were conducted under shear stress–controlled loading conditions. Figure 6 shows the results of the shear stress paths in the p-τ-plane and the shear stress-strain in the τ-γ-diagram. The development of pore water pressure (PWP) with the number of cycles is presented in Figure 7.

The model predicts a progressive increase in shear strain as the loading path approaches the failure envelope. The simulations in the τ-γ-plots show well-defined hysteresis loops. For R10 (Figure 6c and 6d) with the smallest cyclic amplitude of $\tau^{ampl} = 6.5$ kPa, the simulation reproduces relatively narrow hysteresis loops, indicating small shear strain. With increasing loading amplitude (see R11 to R12, Figure 6c to 6f), the hysteresis loops widen, and the shear strain amplitudes become larger. Nevertheless, the hysteresis loops with increasing cycles are not seen in the experimental curves.

Figure 7 displays the simulated normalized excess pore water pressures compared to the experiments. The simulations capture the PWP accumulation well, with the best overall agreement across all considered experimental results. In some cases, the simulations predict liquefaction that was not observed in the experiments data, as the laboratory test R11 and R12 had to be terminated to avoid damage to the hollow cylinder apparatus. Extrapolation of the accumulated pore water pressure curve from experiment R11 and 12 suggests that liquefaction would likely have occurred after only a few additional cycles.

Table 4. Triaxial tests with regular signal R10-12, initial effective mean pressure p_0 = 100 kPa and isotropic consolidation τ_s = 0 kPa.

Test	R10	R11	R12
D_{r0} [%]	27	33	29
τ^{ampl} [kPa]	6.5	9.5	12.5

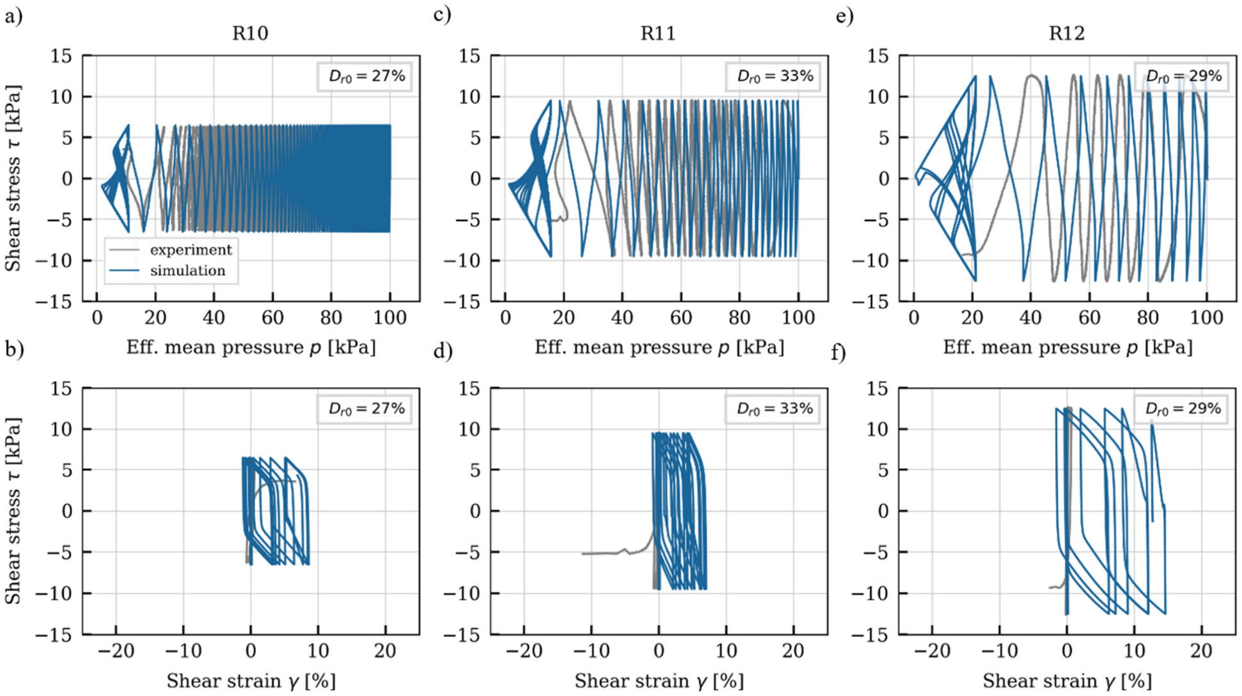

Figure 6. Sanisand simulations (blue) of hollow cylinder triaxial tests R10, R11 and R12 ($D_{r0} \cong 30\%$ and p_0 = 100 kPa) with regular signals τ^{ampl} = of a,b) 6.5 kPa, b,c) 9.5 kPa and c,d) 12.5 kPa.

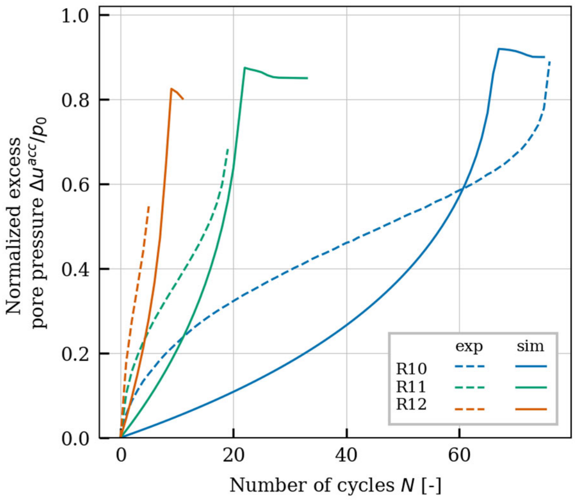

Figure 7. Normalized excess pore water pressure $u^{\text{acc}}(N)/p_0$ from simulations (solid line) and experimental data (dashed lines) for the undrained hollow cylinder triaxial tests.

6 CONCLUSION

For regular loading in the triaxial tests, axial strain remained nearly constant in the initial cycles and rose sharply as the effective stress path approached the failure envelope, particularly in extension. The Sanisand model reproduces the general trends in PWP accumulation and cyclic stiffness decay, with improved PWP agreement at higher amplitudes but a systematic underestimation of number of cycles to liquefaction.

For irregular loading tests, pore water pressure accumulation was generally delayed, while liquefaction tended to be overpredicted. In cases where the experiments did not reach liquefaction (IR15, IR17), the simulations showed a delayed onset followed by a rapid build-up of pore water pressure. In cases where liquefaction occurred in both experiments and simulations (IR16, IR18), the simulated onset was still markedly delayed. Furthermore, the simulations failed to reproduce clearly defined axial strain hysteresis loops, underscoring the model's limitations in capturing soil behavior under irregular loading sequences.

Hollow cylinder simulations show the closest match between simulation and experiment in terms of PWP accumulation, although liquefaction in the simulation is developed more slowly at the beginning, after which the excess pore pressure rises sharply.

Simulations of triaxial tests with the Sanisand model showed that, for these loosely deposited sands, the effective mean pressure dropped to zero, indicating full liquefaction; however, the number of cycles to liquefaction was predicted with limited accuracy, except for the hollow cylinder tests. Overall, while Sanisand captures many qualitative features of cyclic soil response, it shows clear limitations in reproducing irregular excitation patterns and density-dependent cyclic mobility behavior. Future work will employ experimental results to calibrate and assess other advanced constitutive models for soils under regular and irregular loading.

7 REFERENCES

Dafalias, Y. F. & Manzari, M., 2004. Simple plasticity sand model accounting for fabric. Journal of Engineering Mechanics, Issue 130.6, pp. 622-634. https://doi.org/10.1061/(ASCE)0733-9399(2004)130:6(622)

Ishihara, K. & Yasuda, S., 1972. Sand liquefaction due to irregular excitation. Soils and Foundations, 12(4), pp. 65-77.

Ishihara, K. & Yasuda, S., 1975. Sand liquefaction in hollow cylinder torsion unter irregular excitation. Soils and Foundations, 15(1), pp. 45-49.

Knittel, L.; Machaček, J.; Gehring, S.; Raabe, P.; Dahmen, D.; Wichtmann, T.; Stutz, H. H., 2024. Investigations on the liquefaction resistance of an open-cast lignite mine soil under loading by earthquake-typical signals. Geotechnik, 47(3), pp. 212-230. https://doi.org/10.1002/gete.202200015.

Niemunis, A., 2008. Incremental driver user's manual. [Online] Available at: https://soilmodels.com/idriver/

Seed, H. B. & Idriss, I. M., 1971. Simplified procedure for evaluating soil liquefaction potential. Journal of the Soil Mechanics, Band ASCE 107, pp. 1249-1274.

Wichtmann, T., Fuentes, W. & Triantafyllidis, T., 2019. Inspection of three sophisticated constitutive models based on monotonic and cyclic tests on fine sand: Hypoplasticity vs. Sanisand vs. ISA. Soil Dynamics and Earthquake Engineering, Issue 124, pp. 172-183. https://doi.org/10.1016/j.soildyn.2019.05.001